



Cite this: *Digital Discovery*, 2023, **2**, 1089

Received 26th January 2023  
Accepted 16th June 2023

DOI: 10.1039/d3dd00010a  
[rsc.li/digitaldiscovery](http://rsc.li/digitaldiscovery)

## Introduction

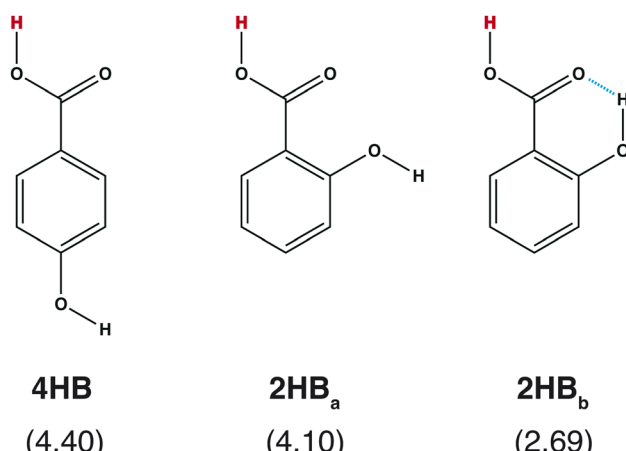
What is required for good features in molecular graph neural networks (GNNs)? Several studies have been conducted concerning feature selection in data science, and it has been mentioned that good features should improve accuracy, overcorrelation, and interpretability.<sup>1–3</sup> Recently, GNNs and graph convolutional networks (GCNs) have been widely applied in chemistry.<sup>4–7</sup> Feature selection should also be discussed in detail from the chemistry viewpoint in order to enhance the performance of the GNNs and GCNs in the field of chemistry.

Accuracy is one of the most important points in feature selection. In chemistry, a small structural difference affects the molecular properties. For example, the acid dissociation constant is greatly affected by the positions of the functional groups. Scheme 1 shows three hydroxybenzoic acid (HB) structures. The difference is only the relative positions of the OH and COOH groups, and the orientation of the OH group. Despite the small difference, these conformations give different  $pK_a$  values ( $= -\log K_a$ ), where  $K_a$  is the acid dissociation constant. Good features should have the ability to distinguish the difference.

Overcorrelation is another critical point in GNN and GCN studies. The overcorrelation in features indicates that they have

irrelevant or redundant information.<sup>2,3</sup> Jin *et al.* discussed the GNN performance based on feature overcorrelation. Their model (DeCorr) reduced feature correlation and performed better than the standard GNN approaches.<sup>3</sup> Feature correlation in the convolution step was also focused on the GCN. It was shown that the GCN shows the degradation of the performance when the correlation of the features between the layers becomes large.<sup>9,10</sup> Thus, the overcorrelation in the features should be removed in molecular GNNs.

Accuracy and overcorrelation are important points in feature selection. However, in chemistry, interpretability is considered more seriously. Recently, due to the development of theoretical



Graduate School of Arts and Sciences, The University of Tokyo, 3-8-1 Komaba, Meguro-ku, Tokyo 153-8902, Japan. E-mail: [c-d.yokogawa@g.ecc.u-tokyo.ac.jp](mailto:c-d.yokogawa@g.ecc.u-tokyo.ac.jp)

† Electronic supplementary information (ESI) available: Details of the machine learning process, RMSEs of the  $pK_a$  values obtained by IGC and two types of atom features (IAPs and MAPs), which were computed with the Hartree–Fock (HF)/6-31G\*\* level of theory, and experimental and calculated  $pK_a$  values of the test set. See DOI: <https://doi.org/10.1039/d3dd00010a>

Scheme 1 Chemical structures of hydroxybenzoic acid (HB) and  $pK_a$  values computed with a quantum chemical approach<sup>8</sup> in parentheses.



methods and computers, various molecular properties can be computed accurately. However, to understand the chemistry, the reasons behind such physical properties must be investigated. In the quantum chemical field, an analysis of partial charges on the atoms, such as Mulliken and natural population analyses,<sup>11,12</sup> is often applied. If the atomic charges are assigned to each atomic site, the chemists can image the charge flow in a molecule, which leads to the design of new molecules. Therefore, when molecular GNNs and GCNs are applied to chemistry, the obtained results should be explained with the employed features.

In this study, we propose a new feature for molecular GNNs considering accuracy, overcorrelation, and interpretability. In previous studies, most of descriptors employed in chemistry were molecular properties<sup>13,14</sup> or isolated atomic properties<sup>15,16</sup> or both,<sup>17,18</sup> while molecular atomic properties computed with quantum chemical approaches were employed in this study. Although the preparation of the molecular atomic properties computed with quantum chemical calculations requires computational time, we can employ variety of atomic properties as descriptors, such as atomic charges, Fukui function,<sup>19</sup> dispersion coefficients,<sup>20,21</sup> isotropic magnetic shielding constant, and so on, which will be useful for better prediction. In the preparation of feature vectors from the molecular atomic properties, to improve the overcorrelation in GNNs, we employed the concatenation approach. Moreover, by coupling the integrated gradient approach with our model, the interpretability can be discussed based on the atomic site, which is useful in the design of molecules. Here, we evaluate the performance of the proposed model by computing the  $pK_a$  values.

## Method

In this study, we proposed a new feature preparation process and constructed a machine learning (ML) process using the prepared features. Scheme 2 summarizes the flowchart of the present model. The feature preparation process comprises the preparation of atomic properties and concatenation. This section explains each step in detail.

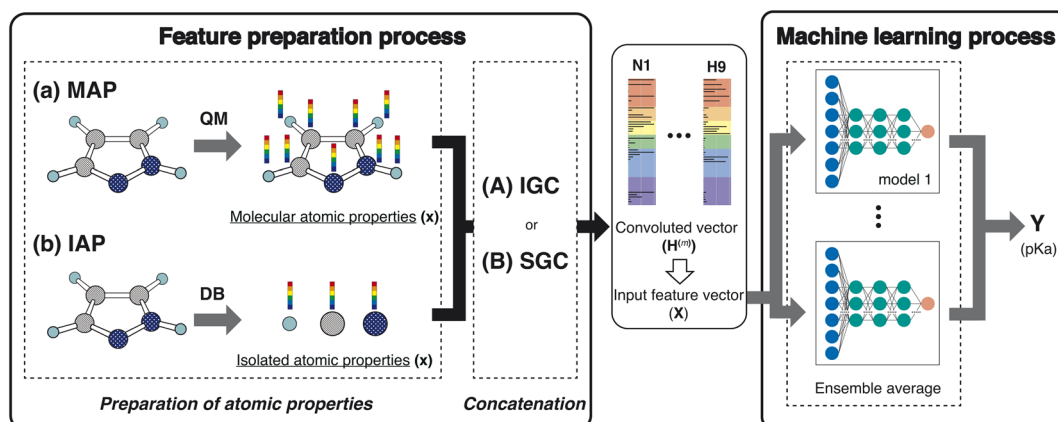
## Preparation of atom properties

Various atom features have been applied in GCN studies.<sup>22,23</sup> For example, Choudhary and DeCost employed the following eight atomic features in their GNN study: electronegativity, group number, covalent radius, valence electrons, first ionization energy, electron affinity, block, and atomic volume.<sup>23</sup> They are isolated atomic properties (IAPs) and can be prepared without molecular information. In the quantum mechanical (QM) field, molecular-atomic properties (MAPs) are also employed for the analysis. After the QM calculations, various atomic properties are assigned to each atomic site using decomposition approaches.<sup>12,20,24,25</sup>

In this study, we used the IAPs and the MAPs in feature preparation. In IAPs, the following six atomic properties were applied: effective nuclear charge, atomic polarizability, atomic radius, ionization energy, electron affinity, and atomic mass. Concerning the MAPs, the following nine properties were used: the positive and negative values of the constrained spatial electron density distribution (cSED) charge ( $Q^+$  and  $Q^-$ ),<sup>25</sup> the positive and negative values of the isotropic magnetic shielding constant ( $\sigma^+$  and  $\sigma^-$ ), the positive and negative values of the molecular electrostatic potential (MEP)<sup>26-28</sup> change at the nucleus ( $M^+$  and  $M^-$ ), the positive value of the partial Fukui function ( $F^-$ ),<sup>19</sup> volume ( $V$ ), and atomic dispersion coefficient ( $C_6$ ).<sup>20,21</sup> Although the partial Fukui function also takes positive and negative values, only the positive value is important. For MEP, the potential negatively increases as the atomic number increases. In order to remove the atomic number dependency of the MEP, the  $M^+$  and  $M^-$  were computed by subtracting the MEP value computed in an isolated atom from the MEP value computed in a molecule.

## Concatenation of atomic properties

To construct the ML features from the atom properties, the GNN was considered. The hidden feature of node  $v$  in the  $l$ -th layer is denoted by  $h_v^{(l)}$  and  $h_v^{(0)} = x_v$ , where  $x$  represents the node features (MAPs or IAPs). Moreover,  $\mathbf{h}^{(l)}$  is formally given along the update step, as follows:



Scheme 2 Schematic of the workflow in this study.



$$\mathbf{h}^{(l)} = U^{(l)}(\mathbf{h}^{(l-1)}), \quad (1)$$

where  $U^{(l)}$  is the update function at the  $l$ -th layer.<sup>29</sup> By concatenating the obtained  $\mathbf{h}^{(l)}$  ( $l = 0, 1, \dots, L$ ), we prepared the following vector:

$$\mathbf{H}^{(L)} \equiv \mathbf{h}^{(0)} \oplus \mathbf{h}^{(1)} \oplus \dots \oplus \mathbf{h}^{(L)} \quad (2)$$

where  $\oplus$  is the concatenation of two vectors. This step is a simple version of jumping knowledge networks.<sup>30</sup> The concatenated vector  $\mathbf{H}^{(L)}$  is the feature vector for the ML process.

Many processes in the update step are given in eqn (1). Concerning the simple graph convolution (SGC),<sup>31</sup> the update step is given as follows:

$$\mathbf{h}^{(l)} = \mathbf{S} \mathbf{h}^{(l-1)} = \mathbf{S}' \mathbf{x} \quad (3)$$

where  $\mathbf{S} = \tilde{\mathbf{D}} - 1/2\tilde{\mathbf{A}}\mathbf{D} - 1/2$ ,  $\tilde{\mathbf{A}} = \mathbf{A} + \mathbf{I}$ ,  $\mathbf{A}$  is the adjacency matrix, and  $\tilde{\mathbf{D}}$  is the degree matrix of  $\tilde{\mathbf{A}}$ . Although the update step with  $\mathbf{S}$  is well employed, it is known that the elements of  $\mathbf{S}'$  converge to a fixed value when  $l$  is large.<sup>32</sup> To overcome this problem, the following update step was proposed:

$$\mathbf{h}^{(l)} = \mathbf{a}^{(l)} \mathbf{x} \quad (4)$$

where  $\mathbf{a}^{(l)}$  is the hollow matrix, and the off-diagonal elements are defined as follows:

$$a_{ij}^{(l)} = \begin{cases} \bar{b}_{ij} & (l = 1) \\ \sqrt{\bar{a}_{ij}^{(l)} \bar{a}_{ji}^{(l)}} & (l > 1) \end{cases} \quad (5)$$

where

$$\bar{a}_{ij}^{(l)} = \delta^H \left( \sum_k \bar{b}_{ik} a_{kj}^{(l-1)}; \max_{m=1, \dots, l-1} a_{ij}^{(m)} \right) \quad (6)$$

and  $\delta^H(x; \lambda)$  is the hard shrinkage function;  $\bar{\mathbf{b}}$  is defined as follows:

$$\bar{\mathbf{b}} = \mathbf{D}^{-1/2} \mathbf{b} \mathbf{D}^{-1/2} \quad (7)$$

where  $\{b_{ij}\}$  is the Wiberg bond index.<sup>33</sup> When  $a_{ij}^{(l)}$  has a nonzero value, the path  $i \leftrightarrow j$  at the  $l$ -th step is either the shortest, or not, but it comprises strong bonds, such as double and triple bonds. Because the shortest path and the path through strong chemical bonds are important to transfer the information to each node, the new convolution process is termed an important graph convolution (IGC).

The employed atomic properties are defined with different units, and the maximum values in the properties differ. To remove the bias, we employed min-max normalization to  $\mathbf{H}^{(L)}$ . The element  $h_i^{(l)}$  ( $0 \leq l \leq L$ ) in  $\mathbf{H}^{(L)}$  was normalized with

$$\tilde{h}_i^{(l)} = \frac{h_i^{(l)}}{h_i^{\max}}, \quad (8)$$

where  $h_i^{\max}$  is the maximum value of the  $i$ -th property determined from the training and validation datasets.

## ML process

To discuss the performance of the prepared features, the supervised learning algorithm for  $pK_a$  recognition was employed. The feature vector  $\mathbf{H}^{(L)}$  of the dissociated proton is chosen as an input vector  $\mathbf{X}^{(0)}$  in the multilayer perceptron (Scheme 2). The output  $\mathbf{Y}$  ( $pK_a$  in this study) is obtained as follows:

$$\mathbf{X}^{(m)} = \sigma(\mathbf{X}^{(m-1)} \Theta^{(m)} + \beta^{(m)}), \quad (9)$$

$$\mathbf{Y} = \mathbf{X}^{(M-1)} \Theta^{(M)} + \beta^{(M)}, \quad (10)$$

where  $\Theta^{(m)}$  and  $\beta^{(m)}$  are the weight matrix and the bias vector of the layer  $m$ , respectively, and  $\sigma$  is a nonlinear activation function, e.g., a ReLU. The number of layer  $M$  is set to 4.

$\mathbf{Y}$  depends on the weight and the hyperparameters, such as the number of nodes in the hidden layers and the dropout ratio. If the weight is optimized with different hyperparameters, different trained networks are produced. A linear combination of the corresponding outputs was taken as follows:<sup>34,35</sup>

$$\bar{\mathbf{Y}} = \sum_j^p \alpha_j \mathbf{Y}_j, \quad (11)$$

where  $\mathbf{Y}_j$  is the output obtained with the  $j$ -th trained network,  $p$  is the number of trained networks, and  $\alpha_j$  is the associated combination weight;  $p = 5$ , and an equal combination-weight was employed. The hyperparameters were chosen from the top five best in the hyperparameter fitting process.

## Computational details

### Datasets

The  $pK_a$  values and molecular information were obtained from the training and test sets prepared in the previous study.<sup>36</sup> The number of molecules in the training and test sets are 2216 and 740, respectively. The datasets employed in this study were carefully cleaned and curated from the training and test sets by adopting the following steps. First, the molecules that have a CAS registry number were selected from the training and test sets. Next, we remove the molecules from the datasets when the  $pK_a$  values are far from those of the analog or the deprotonation site is not clearly identified. In addition, the calculation was restricted to molecules with no iodide atom because of the current program limitation. Finally, 1014 and 316  $pK_a$  values were obtained for the training and test sets, respectively. The training datasets (1014  $pK_a$  values) were divided into training and validation datasets with a 80:20 ratio (811 and 203  $pK_a$  values, respectively).

### Hyperparameters

There are three layers, and the hidden size of the layers is  $n_0$ ,  $n_1$ , and  $n_2$ , respectively, which are summarized in Fig. S1 (ESI†). A hyperparameter search for the optimal hidden size ( $n_0$  and  $n_1$ ) and the dropout rate was computed using Optuna,<sup>37</sup> where the Bayesian hyperparameter optimization was employed. The number of trial steps and epochs were 100 and 3000 epochs,



respectively. The weight was further trained to 8000 epochs to improve its final accuracy.

### Calculations of molecules

The molecular geometries were computed at the CAM-B3LYP/aug-cc-pVDZ level of theory.<sup>38,39</sup> The CSED charge, partial Fukui function, volume, atomic  $C_6$  dispersion coefficient, and MEP were computed using the GAMESS program package,<sup>40</sup> and isotropic magnetic shielding constants on an atom were computed using the Gaussian program package.<sup>41</sup>

The MAPs were also computed at the Hartree–Fock (HF)/6-31G\*\* level of theory. Although a large difference in computational cost exists between HF/6-31G\*\* and CAM-B3LYP/aug-cc-pVDZ, the difference in the predicted  $pK_a$  was small, as shown in Fig. S2 (ESI†).

## Results and discussion

The correlation between features was evaluated using Pearson's correlation coefficient,

$$\rho_{k,l} = \frac{\sum_i \mathbf{t}(\mathbf{h}_i^{(k)} - \bar{\mathbf{h}}^{(k)}) \cdot (\mathbf{h}_i^{(l)} - \bar{\mathbf{h}}^{(l)})}{\sqrt{\sum_i |\mathbf{h}_i^{(k)} - \bar{\mathbf{h}}^{(k)}|^2} \sqrt{\sum_i |\mathbf{h}_i^{(l)} - \bar{\mathbf{h}}^{(l)}|^2}}, \quad (12)$$

where  $\mathbf{h}_i^{(k)}$  is the feature vector in the  $k$ -th layer of the molecular  $i$ , and  $\bar{\mathbf{h}}^{(k)}$  is the mean value of  $\mathbf{h}_i^{(k)}$ . The input feature of molecule  $i$  was prepared by taking the concatenation of  $\{\mathbf{h}_i^{(k)}\}$  (eqn (2) and Scheme 2). A large  $\rho_{k,l}$  means that  $\mathbf{h}_i^{(k)}$  and  $\mathbf{h}_i^{(l)}$  are similar and they have common information, while a small  $\rho_{k,l}$  means that  $\mathbf{h}_i^{(k)}$  and  $\mathbf{h}_i^{(l)}$  have unique information and

their overlap became small. When the common features among  $\mathbf{h}_i^{(k)}$  and  $\mathbf{h}_i^{(l)}$  are repeated in the concatenation (eqn (2)), the concatenated vector  $\mathbf{H}^{(L)}$  and input vector  $\mathbf{X}^{(0)}$  contain the redundant data.<sup>42</sup> In Fig. 1, the heat maps of  $\rho_{k,l}$  computed with IGC and SGC are shown. In the correlation calculations, IAPs and MAPs were employed as the atomic properties. Because  $\mathbf{h}_i^{(0)}$  computed with IAPs have the same values among the molecules, the correlation coefficients ( $\rho_{0,l}$  and  $\rho_{k,0}$ ) cannot be defined, which were colored black in Fig. 1. As shown in Fig. 1(a), the correlation between  $\mathbf{h}^{(0)}$  and  $\mathbf{h}^{(k)}$  ( $k \geq 1$ ) was small in the case of SGC(MAP), whereas the correlations between  $\mathbf{h}^{(k)}$  and  $\mathbf{h}^{(l)}$  ( $k, l \geq 1$ ) were large in both cases of MAPs and IAPs (Fig. 1(a) and (b)). Therefore, the redundancy in the features of constructed  $\mathbf{X}^{(0)}$  should be large when SGC(IAP) is employed. By contrast, the correlation between the  $x$ -th and  $y$ -th layer vectors is small when IGC is chosen (Fig. 1(c) and (d)). From the results, we concluded that the redundancy in the  $\mathbf{X}^{(0)}$  constructed with IGC should be reduced.

It is useful to consider the meaning of the small correlation between  $\mathbf{h}^{(k)}$  and  $\mathbf{h}^{(l)}$  ( $k \neq l$ ) in IGC(MAP) based on spectral filtering. When  $\mathbf{v}_i$  and  $\lambda_i$  are the  $i$ -th eigenvector and eigenvalue of Laplacian, respectively, the spectral filtering on graph signal  $\mathbf{x}$  can be written as follows:

$$\mathbf{y} = \sum_k \mathbf{y}^{(k)}, \quad (13)$$

$$\mathbf{y}^{(k)} \equiv f(\lambda_k) \mathbf{v}_k \mathbf{v}_k^T \mathbf{x} \quad (14)$$

where  $\mathbf{y}$  is the filtered signal and  $f(\lambda_k)$  is the filter kernel. From the definition,  $\mathbf{y}^{(k)}$  and  $\mathbf{y}^{(l)}$  ( $k \neq l$ ) are perpendicular to each other. From the similarity of eqn (4) and (14) and the absence of

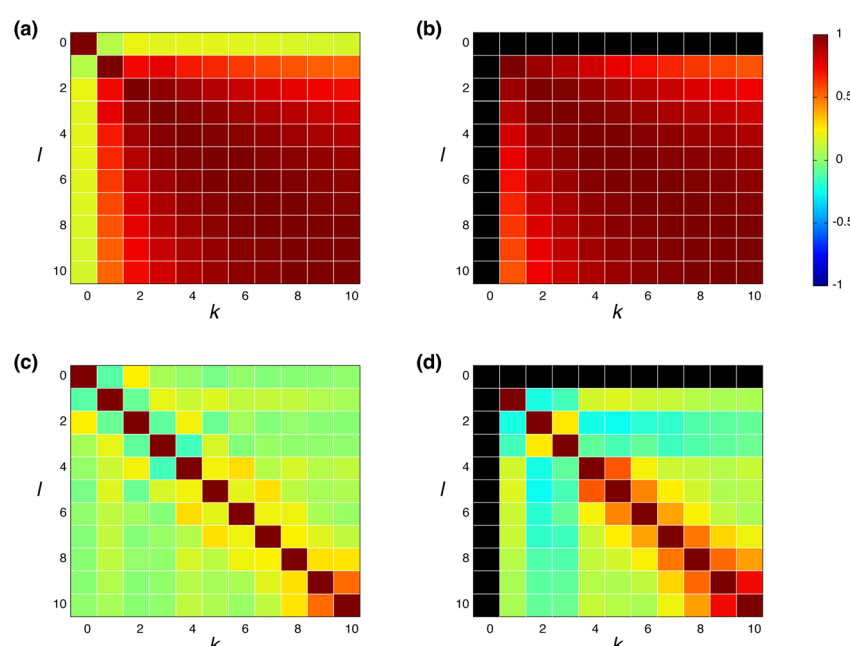
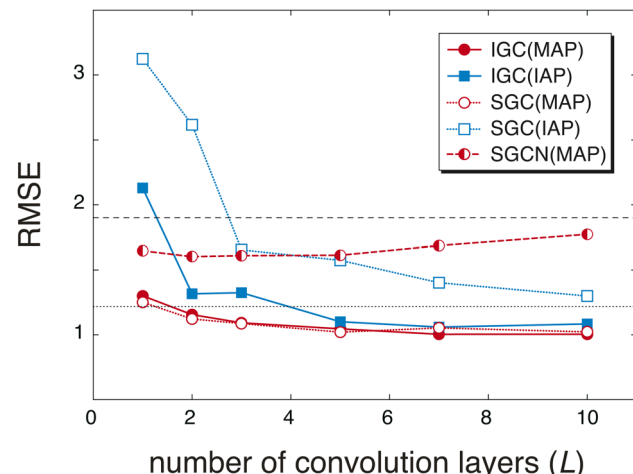


Fig. 1 Heatmap of Pearson's correlation coefficient  $\rho_{k,l}$  between  $\mathbf{h}^{(k)}$  and  $\mathbf{h}^{(l)}$ ,  $\mathbf{h}^{(l)}$  and  $\mathbf{h}^{(k)}$  were prepared with (a and b) SGC and (c and d) IGC. MAPs were employed for (a) and (c), and IAPs were employed for (b) and (d). The pairs with undefined correlation coefficients are shown in black.





**Fig. 2** Root mean square errors (RMSEs) of  $pK_a$  values obtained by two types of atomic features (IAPs and MAPs) and convolution processes (IGC and SGC) with different numbers of convolution layers (1, 2, 3, 5, 7, and 10). In the case of MAPs, the convolution of a simple graph convolution network (SGCN) was also checked. For comparison, the RMSEs computed with MolGpKa and OPERA are also shown with black dashed and dotted lines, respectively.

correlation between  $\mathbf{y}^{(k)}$  and  $\mathbf{y}^{(l)}$  ( $k \neq l$ ),  $\mathbf{h}^{(k)}$  can be considered to be a filtered vector, as in the case of graph spectral filtering.<sup>43</sup>

The redundancy in the feature vector  $\mathbf{X}^{(0)}$  probably affects the accuracy of the predicted  $pK_a$  values. To discuss the relationship between the accuracy and the redundancy in  $\mathbf{X}^{(0)}$ , the root mean square errors (RMSEs) of the  $pK_a$  values were calculated. Because  $\mathbf{X}^{(0)}$  is the concatenated vector  $\mathbf{H}^{(L)}$  of the dissociated proton, the size of  $\mathbf{X}^{(0)}$  is controlled by the convolution layers ( $L$ ). In Fig. 2, the RMSEs computed with  $L = 1, 2, 3, 5, 7$ , and 10 are shown. For comparison, the RMSEs were also computed with a freely available  $pK_a$  prediction tool called OPERA<sup>36</sup> and MolGpKa.<sup>44</sup> In the case of MolGpKa, the model was optimized using the dataset employed in this study. To evaluate the effectiveness of the concatenation in eqn (2), we performed an ablation study about SGC without the concatenated module. In the ablation study,  $\mathbf{S}^L \mathbf{x}$  was employed as the feature vector  $\mathbf{X}^{(0)}$ , which is the analogue of a simplified graph neural network (SGCN).<sup>31</sup> When an IAP was employed, there was a large difference in the accuracy between the convolution approaches, SGC and IGC. Although the error in IGC(IAP) and SGC(IAP) decreases as  $L$  increases, the error in IGC(IAP) is largely improved as  $L$  increases when compared with that in SGC(IAP). This is because the redundancy in  $\mathbf{X}^{(0)}$  of IGC(IAP) is smaller than that of SGC(IAP) (Fig. 1). When a MAP was employed, the RMSE is

small in both cases of IGC and SGC because  $\mathbf{X}^{(0)}$  has unique information even with a small  $L$  value (Fig. 1(a) and (c)). In both cases of SGC and IGC with a concatenated module, the prediction performance was improved up to  $L = 10$ , while the SGCN model with MAPs gave the best performance with  $L = 2$ . This difference shows that the concatenation in eqn (2) plays an important role in accurate prediction.

Although the RMSE shown in Fig. 2 is one of the good properties to discuss accuracy, it is also important to check whether the prepared features can reproduce the  $pK_a$  difference stemming from the structural difference (Scheme 1). In Table 1, the  $pK_a$  values of hydroxybenzoic acids predicted with IGC(MAP), IGC(IAP), SGC(MAP), SGC(IAP), MolGpKa, and OPERA are shown. As a reference, the  $pK_a$  values computed with QM approaches are also shown.<sup>8</sup> The obtained  $pK_a$  values reproduced the  $pK_a$  values computed with the QM, except for MolGpKa. Moreover, IGC(MAP), SGC(IAP), and OPERA can reproduce the QM result where the  $pK_a$  of 4HB is larger than that of 2HB, suggesting that SGC and IGC can include structural isomerism through convolution. However, the  $pK_a$  difference between 2HB<sub>a</sub> and 2HB<sub>b</sub> was reproduced only with IGC(MAP), IGC(IAP), and SGC(MAP). The results show that the IGC(MAP) gave a good feature to reproduce the  $pK_a$  difference stemming from the structural difference.

From the viewpoint of accuracy and the correlation between features, IGC with MAPs is superior to others. However, with accuracy, it is difficult to say if the concatenated vector computed with IGC(MAP) is a good feature. To discuss the interpretability of the IGC(MAP), the integrated gradients (IGs) were computed.

$$IG_i(\mathbf{X}^{(0)}) = \left( X_i^{(0)} - \bar{X}_i^{(0)} \right) \int_{\alpha=0}^1 \frac{\partial F\left( \bar{\mathbf{X}}^{(0)} + \alpha(\mathbf{X}^{(0)} - \bar{\mathbf{X}}^{(0)}) \right)}{\partial X_i} d\alpha, \quad (15)$$

where  $F$  represents the machine learning process shown in Scheme 2,  $\mathbf{X}^{(0)}$  is the concatenated vector of a dissociated proton, and  $\bar{\mathbf{X}}^{(0)}$  is the baseline. Although it is well known that the baseline is important in calculating IGs, there is no universal rule to define the baseline. It is also difficult to determine the baseline of  $pK_a$ . As shown in a previous study,<sup>36</sup> most of the DataWarrior acidic  $pK_a$  values, which are a freely available  $pK_a$  dataset,<sup>45</sup> are within the range ( $0 < pK_a < 14$ ). Therefore, the middle of the  $pK_a$  range ( $pK_a = 7$ ) is a candidate for the baseline. In this study, the  $\mathbf{H}$ -value of 4-nitrophenol was chosen as the baseline  $\bar{\mathbf{X}}^{(0)}$  in eqn (15) because the  $pK_a$  value is close to 7. With this baseline, we can say that the positive  $IG_i$  suggests that the  $i$ -th feature contributes to less acidic character

**Table 1**  $pK_a$  of 4HB, 2HB<sub>a</sub>, and 2HB<sub>b</sub> computed with IGC, SGC, MolGpKa, and OPERA. For comparison, the QM data computed in a previous study were also shown.<sup>8</sup> In IGC and SGC, IAPs and MAPs were employed as atomic properties and the number of layers is 10

|                  | IGC(MAP) | IGC(IAP) | SGC(MAP) | SGC(IAP) | MolGpKa | OPERA | QM   |
|------------------|----------|----------|----------|----------|---------|-------|------|
| 4HB              | 3.58     | 4.00     | 3.46     | 3.93     | 7.61    | 4.47  | 4.40 |
| 2HB <sub>a</sub> | 3.23     | 4.10     | 3.47     | 3.42     | 7.88    | 3.53  | 4.10 |
| 2HB <sub>b</sub> | 1.71     | 3.97     | 2.49     | 3.42     | 7.88    | 3.53  | 2.69 |



( $pK_a > 7$ ) and the negative  $IG_i$  suggests that the  $i$ -th feature contributes to more acidic character ( $pK_a < 7$ ).

Fig. 3(a) summarizes the IGs of 4HB, 2HB<sub>a</sub>, and 2HB<sub>b</sub> computed with the baseline. Because the  $pK_a$  values of 4HB, 2HB<sub>a</sub>, and 2HB<sub>b</sub> are  $<7$ , the negative IGs are important. Fig. 3(a) shows that the difference among the molecules mainly comes from the properties,  $M^+$  ( $k = 0$ ) and  $M^+$  ( $k = 2$ ), where  $M^+$  is the positive MEP value. Previous studies<sup>27,28</sup> have shown that the MEP had a strong negative correlation with the sum of valence natural atomic orbital energies. Therefore, the IGs in Fig. 3(a) show that the  $pK_a$  value decreases as the atomic orbital energy becomes increasingly negative. Because the electron-withdrawing atom makes the atomic orbital energy of the next atom more negative, the IGs in Fig. 3(a) also indicate that the  $pK_a$  value decreases when the sites of  $k = 0$  and 2 are surrounded by the more electron-withdrawing atoms.

As shown in Scheme 3(a), in the case of 2HB<sub>a</sub>, and 2HB<sub>b</sub>, the sites of  $k = 0$  and 2 are the proton H and carbonyl C sites, respectively. When the chemical structure is considered, the carbonyl O atom of 2HB<sub>b</sub> can withdraw the electron on the

carbonyl C atom more strongly than that of 2HB<sub>a</sub>. From the  $pK_a$  difference between 2HB<sub>a</sub> and 2HB<sub>b</sub>, and Scheme 3(a), the explanation by IGs is reasonable.

Although the interpretation in Scheme 3(a) is reasonable for an acidic compound (2HB), checking the interpretation along the  $pK_a$  value is also important. To discuss the interpretation change, the average of IGs in the three  $pK_a$  ranges ( $pK_a < 4$ ,  $4 \leq pK_a < 10$ , and  $10 \leq pK_a$ ) was obtained. In Fig. 3(b), the averaged IGs are shown. Although the averaged IGs in the range  $pK_a < 4$  are similar to those in Fig. 3(a), the averaged IGs in the range  $10 \leq pK_a$  differ totally from those in Fig. 3(a). Under weak acid conditions ( $10 \leq pK_a$ ), the IGs of  $M^+$  ( $k = 0$ ) and  $M^-$  ( $k = 1$ ) are positively large. The obtained IG is reasonable because of the following reasons. When the  $M^+$  and  $M^-$  values increase, the orbital energy difference decreases (Scheme 3(b)), and the polarity of the bond decreases. The large positive IG suggests that the low polarity in the chemical bond makes the  $pK_a$  value positive (less acidic), which is reasonable from the chemical viewpoint, if the size effect is omitted. Scheme 3 shows that the ML model obtained with IGC(MAP) gives a reasonable interpretation for chemists.

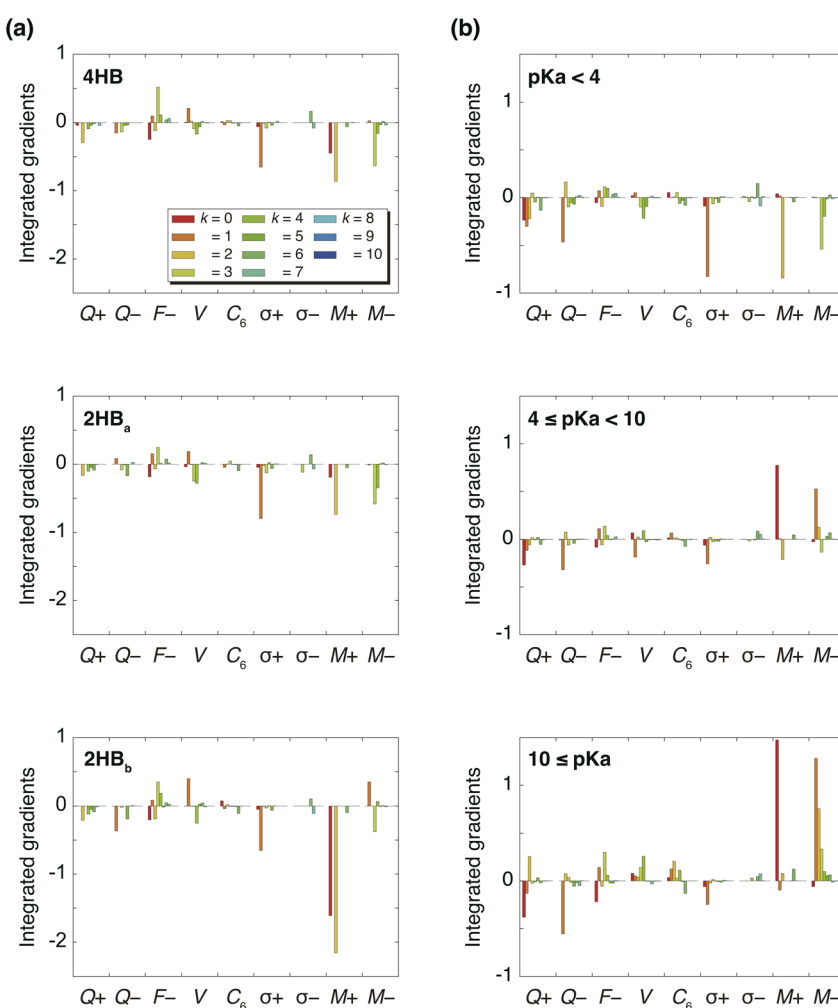
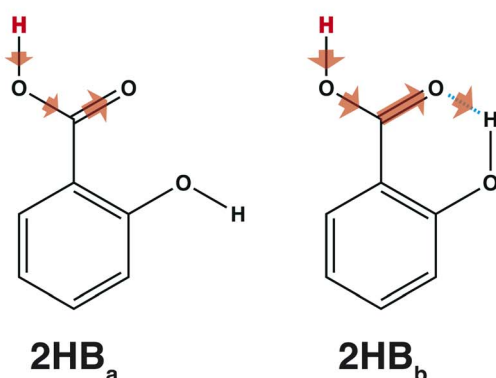


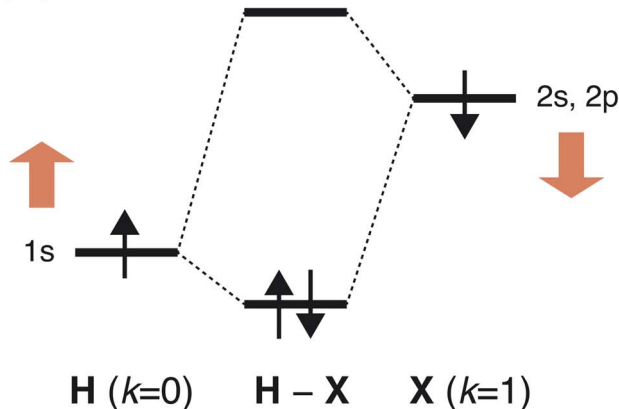
Fig. 3 (a) Integrated gradients on the carboxylic acid hydrogen site of hydroxybenzoic acids (4HB, 2HB<sub>a</sub>, and 2HB<sub>b</sub>) for  $k = 10$  and (b) integrated gradients for  $k = 10$  averaged in three  $pK_a$  ranges ( $pK_a < 4$ ,  $4 \leq pK_a < 10$ , and  $10 \leq pK_a$ ). Moreover, 4-nitrophenol was employed for the baseline molecules.



(a)



(b)



**Scheme 3** (a) Interpretation of the  $pK_a$  difference between  $2\text{HB}_a$  and  $2\text{HB}_b$  derived from IGs. The deprotonated site is colored red, and the arrow size shows the electron-withdrawing strength schematically. (b) Interpretation of a large  $pK_a$  value in the range ( $10 \leq pK_a$ ) based on the chemical bonding between the H and X atoms. The chemical bond ( $\text{H}-\text{X}$ ) comprises the 1s orbital on the H site and 2s, and 2p orbitals on the X site. The red arrows indicate orbital energy changes induced by increased  $M^+$  and  $M^-$  values.

## Conclusions

In this study, a new feature in molecular GNNs was proposed, and the accuracy, overcorrelation between features, and interpretability were discussed in detail. The overcorrelation and accuracy indicate that the IGC with MAPs is superior to others. The prediction output with the IGC(MAP) was analyzed using the IG method. From the analysis, positive values of MEP ( $k = 0$  and 2) are important under acidic conditions, whereas the positive value of MEP ( $k = 0$ ) and the negative value of MEP ( $k = 1$ ) are important under basic conditions, which leads to a reasonable interpretation from a chemistry viewpoint.

In this study, a part of the concatenated vectors  $\{\mathbf{H}^{(L)}\}$  was employed in the ML model. In the future study, we will employ all  $\{\mathbf{H}^{(L)}\}$  in a molecule to construct the ML model for predicting molecular properties, such as the solvation free energy and octanol/water partition coefficient.

## Data availability

The program to predict  $pK_a$  from the concatenated vector  $\mathbf{H}^{(L)}$  is available as open access *via* GitHub ([https://github.com/dyokogawa/pKa\\_prediction](https://github.com/dyokogawa/pKa_prediction)). The training, validation, and test sets used in this paper were also included in the repository (Opt1\_acidic\_tr.csv and Opt1\_acidic\_tst.csv).

## Author contributions

D. Y. developed the theoretical formalism and the programs and performed the predictions. D. Y. and K. S. performed the quantum chemical calculations for the preparation of atomic features using CAM-B3LYP/aug-cc-pVDZ and HF/6-31G\*\*, respectively. Both authors contributed to the final version of the manuscript.

## Conflicts of interest

There are no conflicts to declare.

## Acknowledgements

This study was supported by JST, PRESTO Grant Number JPMJPR21C9, and the Leading Initiative for Excellent Young Researchers. We also acknowledge Enago (<https://www.enago.jp>) for the English language review.

## References

- 1 A.-C. Haury, P. Gestraud and J.-P. Vert, The Influence of Feature Selection Methods on Accuracy, Stability and Interpretability of Molecular Signatures, *PLoS One*, 2011, **6**, e28210.
- 2 D. B. Acharya and H. Zhang, Feature Selection and Extraction for Graph Neural Networks, in *Proceedings of the 2020 ACM Southeast Conference*, 2019, pp. 252–255.
- 3 W. Jin, X. Liu, Y. Ma, C. Aggarwal and J. Tang, Feature Overcorrelation in Deep Graph Neural Networks, *Proceedings of the 28th ACM SIGKDD Conference on Knowledge Discovery and Data Mining*, 2022.
- 4 S. Ishida, K. Terayama, R. Kojima, K. Takasu and Y. Okuno, Prediction and Interpretable Visualization of Retrosynthetic Reactions Using Graph Convolutional Networks, *J. Chem. Inf. Model.*, 2019, **59**, 5026–5033.
- 5 R. Kojima, S. Ishida, M. Ohta, H. Iwata, T. Honma and Y. Okuno, kGCN: a graph-based deep learning framework for chemical structures, *J. Cheminf.*, 2020, **12**, 32.
- 6 M. Jiang, Z. Li, S. Zhang, S. Wang, X. Wang, Q. Yuan and Z. Wei, Drug-target affinity prediction using graph neural network and contact maps, *RSC Adv.*, 2020, **10**, 20701–20712.
- 7 A. Kensert, R. Bouwmeester, K. Elthymiadis, P. Van Broeck, G. Desmet and D. Cooter, Graph Convolutional Networks for Improved Prediction and Interpretability of Chromatographic Retention Data, *Anal. Chem.*, 2021, **93**, 15633–15641.





8 T. Baba, T. Matsui, K. Kamiya, M. Nakano and Y. Shigeta, A density functional study on the pKa of small polyprotic molecules, *Int. J. Quantum Chem.*, 2014, **114**, 1128–1134.

9 Q. Li, Z. Han, X.-M. Wu, Deeper Insights into Graph Convolutional Networks for Semi-Supervised Learning, in *Proceedings of the Thirty-Second AAAI Conference on Artificial Intelligence*, 2018, pp. 3538–3545.

10 M. Chen, Z. Wei, Z. Huang, B. Ding and Y. Li, Simple and Deep Graph Convolutional Networks, *Proceedings of the 37th International Conference on Machine Learning*, 2020, pp. 1725–1735.

11 R. S. Mulliken, Electronic population analysis on LCAO-MO molecular wave functions. I, *J. Chem. Phys.*, 1955, **23**, 1833–1840.

12 A. E. Reed, R. B. Weinstock and F. Weinhold, Natural population analysis, *J. Chem. Phys.*, 1985, **83**, 735–746.

13 B. Huang and O. A. von Lilienfeld, Communication: Understanding molecular representations in machine learning: The role of uniqueness and target similarity, *J. Chem. Phys.*, 2016, **145**, 161102.

14 F. Pereira, K. Xiao, D. A. R. S. Latino, C. Wu, Q. Zhang and J. Aires-de Sousa, Machine Learning Methods to Predict Density Functional Theory B3LYP Energies of HOMO and LUMO Orbitals, *J. Chem. Inf. Model.*, 2017, **57**, 11–21.

15 J. P. Janet and H. J. Kulik, Resolving Transition Metal Chemical Space: Feature Selection for Machine Learning and Structure–Property Relationships, *J. Phys. Chem. A*, 2017, **121**, 8939–8954.

16 K. T. Schütt, M. Gastegger, A. Tkatchenko, K. R. Müller and R. J. Maurer, Unifying machine learning and quantum chemistry with a deep neural network for molecular wavefunctions, *Nat. Commun.*, 2019, **10**, 5024.

17 Y. Zhuo, A. Mansouri Tehrani and J. Brgoch, Predicting the Band Gaps of Inorganic Solids by Machine Learning, *J. Phys. Chem. Lett.*, 2018, **9**, 1668–1673.

18 J. Jiménez-Luna, M. Skalic, N. Weskamp and G. Schneider, Coloring Molecules with Explainable Artificial Intelligence for Preclinical Relevance Assessment, *J. Chem. Inf. Model.*, 2021, **61**, 1083–1094.

19 F. Jensen, *Introduction to Computational Chemistry*, John Wiley and Sons, Chichester, 2nd edn, 2006.

20 D. Yokogawa, Isotropic Site-Site Dispersion Potential Constructed Using QuantumChemical Calculations and a Gemini Auxiliary Basis Set, *Bull. Chem. Soc. Jpn.*, 2019, **92**, 748–753.

21 D. Yokogawa, Isotropic Site-Site Dispersion Potential Determined from Localized Frequency-Dependent Density Susceptibility, *Bull. Chem. Soc. Jpn.*, 2019, **92**, 1694–1700.

22 B. Ramsundar, P. Eastman, P. Walters, V. Pande, K. Leswing and Z. Wu, *Deep Learning for the Life Sciences*, O'Reilly Media, 2019, <https://www.amazon.com/Deep-Learning-Life-Sciences-Microscopy/dp/1492039837>.

23 K. Choudhary and B. DeCost, Atomistic Line Graph Neural Network for improved materials property predictions, *npj Comput. Mater.*, 2021, **7**, 185.

24 R. F. W. Bader, A quantum theory of molecular structure and its applications, *Chem. Rev.*, 1991, **91**, 893–928.

25 D. Yokogawa and K. Suda, Electrostatic Potential Fitting Method Using Constrained Spatial Electron Density Expanded with Preorthogonal Natural Atomic Orbitals, *J. Phys. Chem. A*, 2020, **124**, 9665–9673.

26 P. Politzer, P. R. Laurence and K. Jayasuriya, Molecular electrostatic potentials: an effective tool for the elucidation of biochemical phenomena, *Environ. Health Perspect.*, 1985, **61**, 191–202.

27 S. Liu, C. K. Schauer and L. G. Pedersen, Molecular acidity: A quantitative conceptual density functional theory description, *J. Chem. Phys.*, 2009, **131**, 164107.

28 S. Liu and L. G. Pedersen, Estimation of Molecular Acidity via Electrostatic Potential at the Nucleus and Valence Natural Atomic Orbitals, *J. Phys. Chem. A*, 2009, **113**, 3648–3655.

29 J. F. Lutzeyer, C. Wu, M. Vazirgiannis, Sparsifying the Update Step in Graph Neural Networks, *Proceedings of Topological, Algebraic and Geometric Learning Workshops*, 2022, pp. 258–268.

30 K. Xu, C. Li, Y. Tian, T. Sonobe, K.-i. Kawarabayashi, and S. Jegelka, Representation Learning on Graphs with Jumping Knowledge Networks, *Proceedings of the Thirty-Fifth International Conference on Machine Learning*, 2018, pp. 5453–5462.

31 F. Wu, T. Zhang, A. H. d. Souza, C. Fifty, T. Yu, and K. Q. Weinberger, Simplifying Graph Convolutional Networks, *Proceedings of the Thirty-Sixth International Conference on Machine Learning*, 2019, pp. 6861–6871.

32 X. Liu, F. Lei, G. Xia, Y. Zhang and W. Wei, AdjMix: simplifying and attending graph convolutional networks, *Complex Intell. Syst.*, 2022, **8**, 1005–1014.

33 K. B. Wiberg, Application of the Pople-Santry-Segal CNDO method to the cyclopropylcarbinyl and cyclobutyl cation and to bicyclobutane, *Tetrahedron*, 1968, **24**, 1083–1096.

34 S. Hashem and B. Schmeiser, Improving model accuracy using optimal linear combinations of trained neural networks, *IEEE Trans. Neural Networks*, 1995, **6**, 792–794.

35 S. Hashem, Optimal Linear Combinations of Neural Networks, *Neural Networks*, 1997, **10**, 599–614.

36 K. Mansouri, N. F. Cariello, A. Korotcov, V. Tkachenko, C. M. Grulke, C. S. Sprinkle, D. Allen, W. M. Casey, N. C. Kleinstreuer and A. J. Williams, Open-source QSAR models for pKa prediction using multiple machine learning approaches, *J. Cheminf.*, 2019, **11**, 60.

37 T. Akiba, S. Sano, T. Yanase, T. Ohta and M. Koyama, Optuna: A Next-generation Hyperparameter Optimization Framework, *Proceedings of the 25th ACM SIGKDD International Conference on Knowledge Discovery and Data Mining*, 2019.

38 T. Yanai, D. P. Tew and N. C. Handy, A new hybrid exchange-correlation functional using the Coulomb-attenuating method (CAM-B3LYP), *Chem. Phys. Lett.*, 2004, **393**, 51–57.

39 R. A. Kendall, T. H. Dunning Jr and R. J. Harrison, Electron affinities of the first-row atoms revisited. Systematic basis sets and wave functions, *J. Chem. Phys.*, 1992, **96**, 6796–6806.

40 M. W. Schmidt, K. K. Baldridge, J. A. Boatz, S. T. Elbert, M. S. Gordon, J. H. Jensen, S. Koseki, N. Matsunaga,

K. A. Nguyen, S. Su, T. L. Windus, M. Dupuis and J. A. Montgomery, General atomic and molecular electronic structure system, *J. Comput. Chem.*, 1993, **14**, 1347–1363.

41 M. J. Frisch, *et al.*, *Gaussian 16 Revision A.03*, Gaussian Inc., Wallingford CT, 2016.

42 K. Zhang, Z. Li, F. Zhang, W. Wan and J. Sun, Pan-Sharpening Based on Transformer With Redundancy Reduction, *IEEE Geosci. Rem. Sens. Lett.*, 2022, **19**, 1–5.

43 F. Opolka, Y.-C. Zhi, P. Lió and X. Dong, Adaptive Gaussian Processes on Graphs *via* Spectral Graph Wavelets, *Proceedings of The 25th International Conference on Artificial Intelligence and Statistics*, 2022, pp. 4818–4834.

44 X. Pan, H. Wang, C. Li, J. Z. H. Zhang and C. Ji, MolGpka: A Web Server for Small Molecule pKa Prediction Using a Graph-Convolutional Neural Network, *J. Chem. Inf. Model.*, 2021, **61**, 3159–3165.

45 T. Sander, J. Freyss, M. von Korff and C. Rufener, DataWarrior: An Open-Source Program For Chemistry Aware Data Visualization And Analysis, *J. Chem. Inf. Model.*, 2015, **55**, 460–473.

